



**Chiral topological whispering gallery modes formed by gyromagnetic photonic crystals**Yongqi Chen, Nan Gao, Guodong Zhu , and Yurui Fang \**School of Physics, Dalian University of Technology, Dalian 116024, People's Republic of China*

(Received 9 August 2023; revised 1 November 2023; accepted 2 November 2023; published 17 November 2023)

We explore a hexagonal cavity that supports chiral topological whispering gallery (CTWG) modes, which are formed by a gyromagnetic photonic crystal. This mode represents a unique type of topologically protected state, displaying chirality in its propagation within photonic crystals. Finite element method simulations demonstrate the presence of discrete edge states within the topological band gap, arising from the coupling of chiral edge states and whispering gallery modes. Since the cavity exclusively supports edge state modes with group velocity in one direction, it can generate purely traveling modes and remains immune to interference modes. Furthermore, we introduced defects and disorder to assess the cavity's robustness, showcasing the effective maintenance of CTWG modes under various perturbations. Our topological cavity platform offers useful prototype of robust topological photonic devices. The existence of this mode can have important implications for applications such as topological traveling wave devices and efficient optical couplers.

DOI: [10.1103/PhysRevB.108.195423](https://doi.org/10.1103/PhysRevB.108.195423)**I. INTRODUCTION**

Topological photonics provides an exploration realm for manipulating the light-matter interaction through its protected topological photonic states in designing photonic crystals (PCs) [1,2], and becomes a flourishing field and a leading platform for the exploration of phenomenon of nanophotonics [3–8]. Originating from condensed matter physics [9–11], photonic crystals analogous to “edge states” (ESs) of a quantum Hall effect, topological photonics offers particularly exciting opportunities to enable robust propagation and resilience to noise and disorder. The special properties of topological photonics arise from their boundary topology, where the movement of light waves is restricted to certain paths known as ESs, which can support robust light-wave propagation immune to backscattering and perturbations, having potential applications in elevating transmission quality and efficiency of optical signals. The boundary supports antidirection propagation of ESs with different pseudospin by considering the preserved time-reversal symmetry, and has been used in nanocavity, lasers, and so on [12–16]. Applying an external DC magnetic field will induce strong gyromagnetic anisotropy, which will break the time-reversal symmetry (TRS) so that the topological photonics will only support one-way propagation of light, known as the chiral edge state (CES) [17,18]. An experimental demonstration of CESs in microwaves was performed in the seminal work using gyromagnetic photonic crystals immersed in an external DC magnetic field named as magneto-optical photonic crystal (MOPC) [19]. The working frequency even extends to the infrared wavelength [20], which will contribute to future on-chip optical communications and ultrafast information processing. Currently, the CES with broken TRS inspires nu-

merous interesting phenomena, such as nonreciprocal laser in topological cavities with arbitrary geometric shapes [21], group-dispersionless slow light waveguides [22], and unidirectional guided waves [23–25].

Through the ingenious integration of photonic crystal path-closed structures, whispering gallery (WG) modes that confine light beams have been achieved in PCs along near-closed geometric paths. These modes offer significant advantages, including high-quality factors ( $Q$ ) and small mode volumes ( $V$ ), especially in various types of laser resonators, resulting in a substantial enhancement of light-matter interaction [26–30]. The hybrid nature of the PC, which combines light and matter interactions, provides a unique avenue for merging WG modes and edge states to explore topological effects in arrays of resonators. These combination strategies promise to reveal rich and characteristic phenomena in topological isolator photonics. Notably, a recent innovation introduced a honeycomb topological WG cavity, achieved through the fusion of topological photonic crystals and the geometric shape of WG mode cavities. This cavity preserves TRS using the optical quantum spin Hall effect [31,32]. Unlike traditional WG cavities, the confinement of light at the edges of the topological WG cavity does not rely on total internal reflection but rather involves a topological edge transport process. The resulting laser nanocavity exhibits high coherence, extremely low transmission loss, supports single-mode operation, and enables robust optical transport. This technology has been applied to explore cavity quantum electrodynamics and develop high-performance lasers [12,33–36].

In the above research, where the system preserves TRS, the unidirectional transmission of light within the cavity experiences a significant reduction as lattice disorder increases. The size mismatch between the topological nontrivial lattice and the trivial lattice is required to construct the topological interface of the WG cavity, which breaks the lattice symmetry and makes the robustness of the cavity difficult to guarantee.

\*Corresponding author: [yrfang@dlut.edu.cn](mailto:yrfang@dlut.edu.cn)

In such systems, the edge states within the WG cavity exhibit unidirectional properties but will be susceptible to scattering at the corners. Moreover, due to the presence of defects and corners, the two counterpropagation edge states supported by the system exhibit an increase in degeneracy, leading to interference and the creation of standing modes. In contrast, the above limitations will be minimized by a system that utilizes the broken TRS. Considering the properties of the CES, one expects strictly one-way unidirectional WG modes by combining the CES and whispering gallery cavity. The CES properties ensure that light propagates within the WG only in one direction. The progressive advancement of CESs within the WG during light propagation holds substantial potential in photonics and optoelectronics applications. The evolutions from CES to WGMs offers a comprehensive exploration of topological charges and properties in both theoretical and experimental investigations.

In this paper, we report a topological WG cavity supporting only chiral nondegenerate traveling modes. We explore the evolution of CESs into chiral topological whispering gallery (CTWG) modes by examining the transmission through a hexagonal topological closed interface. Furthermore, we demonstrate a hexagonal cavity that is designed to verify the existence of CTWG modes. This integrated CTWG cavity, carefully engineered to possess precise  $C_6$  symmetry, utilizes a static magnetic field to break TRS, thereby allowing only traveling modes to exist within the cavity. Subsequently, employing the finite element method (FEM), we demonstrate the presence of discrete edge states in the topological band gap, resulting from the coupling of topological edge states with WG modes. Additionally, we effectively forbid the generation of standing modes within the cavity and evaluate the cavity's robustness by introducing defects and disorder. The results indicate that all modes within the cavity are characterized as traveling modes, and that the coupling conditions between the CES and the cavity modes are still satisfied in the presence of disordered perturbations. The proposed CTWG cavity offers a potentially robust platform for the development of topological traveling wave generators, topological photonic circuits, and topological lasers operating in microwave frequencies. These advancements promise enhanced field-matter interactions. The simple structural design of this cavity paves the way for new avenues of research, enabling a comprehensive exploration of the interaction between photonic topological states and cavity modes. Given its operational frequency within the communication band, this interaction is poised to engender a plethora of physical phenomena and practical applications.

## II. RESULTS AND DISCUSSION

### A. Structure of chiral topological whispering gallery cavity

Similar to the nontrivial optical structure by combined WG cavity geometries with photonic topological insulators with TRS [37], Fig. 1(a) illustrates the three-layer geometric configuration of a CTWG cavity with broken TRS. It features parallel gold plates on the top and bottom layers to confine electromagnetic waves in the  $z$  direction. The middle layer comprises a CTWG cavity formed by an array of dielectric pillars arranged in a triangular lattice, including trivial lat-

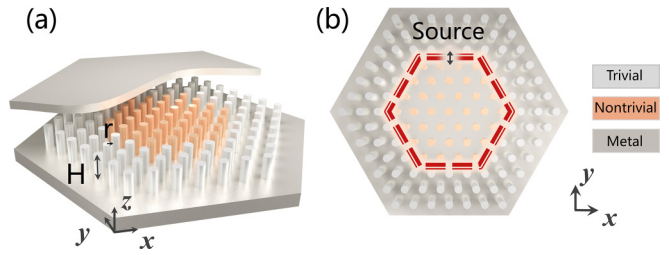


FIG. 1. Chiral topological whispering gallery cavity. (a) The system is a three-layer structure. The middle layer is a topological whispering gallery cavity. The top and bottom layers are parallel copper plates. (b) The top view of the topological whispering gallery cavity. The system is composed of two types of lattices: nontrivial and trivial unit cells highlighted in orange and silver, respectively. The red line marks the topological interface, in which a point source is located.

tice (surrounding) and topological lattice (enclosed within) as shown in Fig. 1(b). The material of the peripheral dielectric pillars (marked in silver) is alumina with  $\epsilon = 10\epsilon_0$  in the air, and the material of the surrounded pillars (marked in orange) is yttrium iron garnet (YIG  $\epsilon = 15\epsilon_0$ ) MOPC, which is used to break the TRS of the system under static external magnetic field (EMF) with an externally applied static EMF,  $\mathbf{H} = H_0\mathbf{e}_z$  ( $H_0 = 1600$  G), where  $\mathbf{e}_z$  is the unit vector perpendicular to the plane of the PC. The static EMF saturates the YIG PC material with spin-magnetic effects, resulting in strong anisotropy and maximum nondiagonal elements of the magnetic permeability tensor, which can be expressed as [18]

$$\boldsymbol{\mu} = \begin{pmatrix} \mu & j\kappa & 0 \\ -j\kappa & \mu & 0 \\ 0 & 0 & 1 \end{pmatrix}, \quad (1)$$

where  $\mu = 1 + \omega_m\omega_0/(\omega_0^2 - \omega^2)$ ,  $\kappa = \omega_m\omega_0/(\omega_0^2 - \omega^2)$  with  $\omega_0 = \gamma H_0$  is the precession frequency,  $\gamma$  is the gyromagnetic ratio,  $H_0$  is the static EMF strength, and  $M_s$  in  $\omega_m = 4\pi\gamma M_s$  describes the saturation magnetization strength.

The hexagonal topological interface formed by splicing the topological lattice and the trivial lattice creates a topological whispering gallery cavity with a perfectly matched  $C_6$  symmetry, as indicated by the red dashed line in Fig. 1(b). The two PCs have different topological invariants, ensuring the formation of robust CES at the topological interface, resulting in a CTWG cavity.

### B. Band structures of topological nontrivial and trivial lattices

Here, topological indices can be used to distinguish topological nontrivial and trivial lattices. Based on the FEM provided by COMSOL MULTIPHYSICS [38], band structure of the two-dimensional (2D) PC in Fig. 1 under  $TM$  polarization are calculated to reveal the topological properties of these two types of PCs in the whispering gallery cavity. To construct the CTWG cavity structure, both the nontrivial and trivial photonic structures with  $a = 3.8$  cm,  $r = 0.122a$ ,  $H = a$  triangular lattice PC slats are selected.

The details of the topological interface formed by the stitching of the two PCs within the cavity are shown in Fig. 2(a). The band structures corresponding to the 2D PCs are

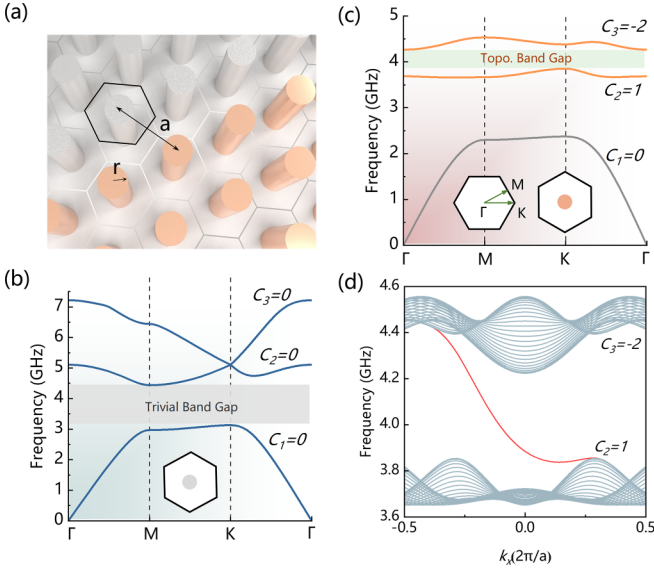


FIG. 2. Band structure and photonic properties of the topological interface. (a) Detailed illustration of the topological interface, composed of topological (orange) and trivial (silver) unit cells of the triangular lattice. They are composed of YIG magneto-optical and alumina PCs respectively. In each unit cell, the lattice constant is  $a = 3.8$  cm, and the dielectric pillar radius is  $r = 0.122a$ . Photonic bands structure of trivial (b) and topological (c) photonic crystals; the insets illustrate the Brillouin zone and the  $k$  path. (d) Projected band diagram. The dispersion curve (red) for the edge state spans the topological band gap.

shown in Fig. 2(b) and 2(c), respectively. The band structure of the alumina photonic crystal is presented in Fig. 2(b). These crystals possess a triangular lattice that creates a broad band gap within the desired frequency range which covers 3.2–4.5 GHz. In Fig. 2(c), the band structure of the MOPC of the triangular lattice YIG pillar is depicted with the second and third bands located at 3.9–4.28 GHz. In this band structure, the energy band is nondegenerated at the  $K$  point. To investigate the topological properties of the MOPC system of broken TRS, the topological invariants of a single band are described by the Chern number [39,40]:

$$C^{(n)} = \frac{1}{2\pi} \int_{\text{BZ}} \mathbf{F}_n(\mathbf{k}) d\mathbf{k} = \frac{1}{2\pi} \int_{\text{BZ}} \nabla_{\mathbf{k}} \times \mathbf{A}_n(\mathbf{k}) d\mathbf{k}. \quad (2)$$

Here, the  $\mathbf{F}_n(\mathbf{k})$  is the Berry curvature.  $\mathbf{A}_n(\mathbf{k}) = -i\langle \mathbf{u}_{n,e,\mathbf{k}} | \nabla_{\mathbf{k}} | \mathbf{u}_{n,e,\mathbf{k}} \rangle$  is the Berry connection. The Chern number of the  $n$ th band is an integer that can be calculated from the integral of the Berry curvature over the first Brillouin zone (see the Methods section).

In the presence of an EMF, as depicted in Fig. 2(c), it is evident that the second and third bands exhibit a gap (indicated by the green-shaded region) within the desired frequency range. The sum of the Chern numbers corresponding to the bands below the band gap is  $|\sum C_{\text{gap}}| = 1$ , so the band gap with nonzero Chern numbers is a topological nontrivial band gap. This topological property is due to the TRS breaking of MOPC under an EMF, which makes the medium have gyromagnetic anisotropy. While Fig. 2(c) exclusively portrays a subset of bands and their corresponding Chern numbers, it is

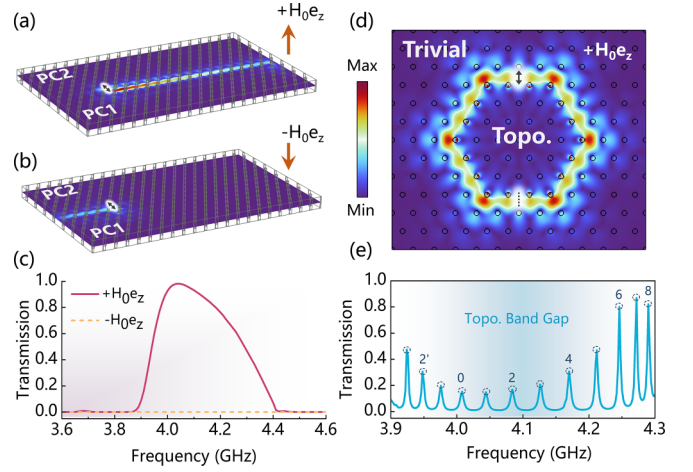


FIG. 3. Evolution of chiral edge states to CTWG modes. The boundary between these two types of PCs with overlapping band gaps supports CES propagating to the right (a) or left (b), depending on the direction of the EMF. The black double arrow indicates the source. (c) The transmission spectrum shows the continuous peaks of the edge states for two opposite values of the EMF. (d) The eigenmode electric field distribution at 4.245 GHz of the CTWG modes with an EMF of  $+H_0 e_z$ . The dotted line draws the position of the detector. (e) The transmission spectra exhibit discrete peaks corresponding to the CTWG modes situated within the topological band gap, thereby signifying the transformation of the continuous CES into discrete CTWG modes.

imperative to acknowledge that the sum of the Chern number over all bands in the system is zero. In Fig. 2(b), calculations indicate that the sum of the Chern numbers is zero for the bands below the alumina pillar PC gap, called the trivial band gap.

To confirm the presence of CES at the topological boundary created by the two PCs, a projected band diagram is generated through numerical simulation of the frequencies for the calculated topological nontrivial band gap, as illustrated in Fig. 2(d). This results in the observation of a CES dispersion curve with a nonzero group velocity [indicated by the red curve in Fig. 2(d) across the topological band gap]. The direction of the group velocity of this edge state is dependent on the magnetic field direction in the vertical plane. As the band gap possesses a nonzero Chern number, the edge state on this interface is protected by the topology. Experimental and theoretical simulations have demonstrated that this chiral topological edge state is robust against certain impurity defects and backscattering [41,42]. This advantage will be utilized in the construction of a whispering gallery cavity based on the chiral topological edge state.

### C. Topological whispering gallery modes based on chiral edge states

The presence of topological edge states with chirality will be confirmed at the interface of the two above PCs. These crystals have been selected to operate within the microwave regime, effectively covering their respective band gaps, and seamlessly stitched together to create the topological interface. As shown in Fig. 3(a), a light source (the black double arrows) with a wavelength within the topological band gap



is positioned at the interface of two PCs possessing distinct topological properties. When the static EMF direction is  $+\mathbf{e}_z$ , the energy of the light source is significantly confined at the topological interface and is transmitted towards the right. However, when the direction of the EMF is reversed to  $-\mathbf{e}_z$ , such as that shown in Fig. 3(b), the wave propagating towards the right is prohibited. This observation confirms the presence of a CES. The normalized transmission spectra measured at the extreme right for two different magnetic field orientations are shown in Fig. 3(c). The transmittance ( $T = P_{\text{out}}/P_{\text{in}}$ ) is calculated by obtaining the time-averaged power flow  $P$  at the port. When the magnetic field direction is  $+\mathbf{e}_z$ , a transmission peak appears at 4.03 GHz, and the entire transmission peak corresponds to the eigenfrequency of the nontrivial band gap of the topological edge state. When reversing the magnetic field direction, however, the rightmost transmission disappears, and transmission to the right is forbidden, further demonstrating the existence of a chiral edge state.

The CTWG cavity can be conceptualized as a closed profile created by the topological interface after undergoing six  $60^\circ$  turns. It is worth noting that the cavity structure can theoretically adopt various closed shapes. In Fig. 3(d), the electric field distribution of the eigenmode is at 4.245 GHz within the hexagonal whispering gallery, with the excitation frequency of the light source situated within the topological band gap. In the same platform as the above illustration (Fig. 1), the side length of the whispering gallery cavity is  $4a$  and the internal topological nontrivial photonic crystal is surrounded by the trivial photonic crystals. The dotted line in the figure indicates the positions of the detector. Numerical simulations indicate that the impact of light propagation through a  $60^\circ$  turn angle is negligible, and the field energy is significantly concentrated within the whispering gallery cavity. The scattering of the corner defect is avoidable in the CTWG. When the EMF is oriented in the  $+\mathbf{e}_z$  direction, the CES, which initially propagates towards the right, transforms into a clockwise mode within the whispering gallery cavity. These cavity modes arise because of coupling of the cavity and the CES propagating around the cavity. To demonstrate this property, the same point source utilized in Fig. 3(a) was positioned within the CTWG cavity, and the transmission spectrum to the symmetric position of the other side of the hexagon was computed, as depicted in Fig. 3(e). When a topological edge state is coupled into a whispering gallery cavity, its transmission exhibits a distinctive interference effect that produces multiple sharp peaks. Each peak corresponds to a topological whispering gallery mode and all these peaks are located within the topological band gap. The emergence of discrete CTWG modes is a distinctive feature of the CES interaction with the cavity mode. The presence of multiple CTWG modes can be attributed to constructive interference in the CES during clockwise transport within the cavity,

$$k_{j/}(\omega)\Lambda = 2m\pi, \quad (3)$$

where  $k_{j/}(\omega)$  is the in-plane wave number corresponding to the CTWG modes,  $\Lambda$  is the circumference of the cavity, and  $m$  corresponds to the number of azimuthal modes. The quantum number  $k_{j/}$  describes the wave number of the CTWG mode at a given perimeter  $\Lambda$  and index  $m$ .

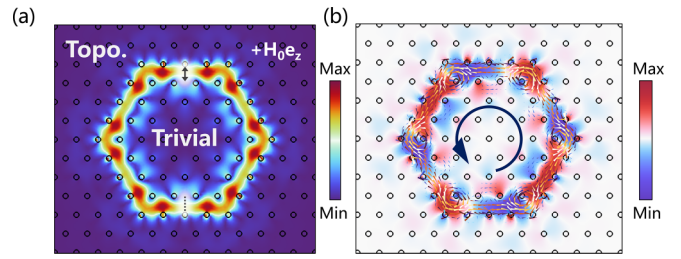


FIG. 4. Topological indices reverse of CTWG cavity. (a) The eigenmode electric field distribution at 4.0906 GHz of the CTWG modes for an EMF of  $+H_0\mathbf{e}_z$ . Compare to (d), when the internal trivial photonic crystals are surrounded by topological nontrivial photonic crystals, resulting in a counterclockwise mode (b) within the whispering gallery cavity. The arrows on the CTWG cavity represent the Poynting vector distribution for the fourth order mode, and the colors show the electric field mode intensity.

To further demonstrate that traveling modes in topological whispering gallery cavity are chiral, we reverse the structure on both sides of the topological interface, where the internal trivial PCs are surrounded by topological nontrivial PCs. Figure 4(a) illustrates the electric field distribution of the eigenmode after reversal, where a cavity mode localized at the interface between the two PCs was observed in the presence of the EMF. Further mapping of the distribution for the time-averaged Poynting vectors ( $\mathbf{S} = \mathbf{E} \times \mathbf{H}$ ) in the topological whispering gallery cavity exhibits evidence that the reversed structure results in a counterclockwise mode, as shown in Fig. 4(b). It is worth noting that all modes within this CTWG cavity are nondegenerate modes due to the broken TRS within the system, which distinguishes them from conventional whispering gallery modes. Especially, the unique cavity modes are all one-way unidirectional which originate from the CES that is the term CTWG modes.

The CTWG cavity in Fig. 3(d) serves as an illustrative example for eigenmodes analysis. The spectrum of the cavity is obtained when the wave vector  $\mathbf{k} = 0$ , as shown in Fig. 5(a). Within the topological band gap, a total of 12 nondegenerate modes are marked (bulk states not shown), evolving from continuous topological edge states into the discrete modes. Figure 5(b) presents the  $E_z$  field distributions of all of these eigenmodes, where one can observe alternating red and blue patterns on the azimuth of the CTWG cavity, also corresponding to the propagation field phase varying of the cavity mode. The 0th mode is marked as 0th in the absence of an azimuthal node, and the corresponding marker for each eigenmode matches the number of CTWG azimuthal modes. The modes above (green dot) and below (purple dot) the 0th CTWG mode corresponds to two orthogonal modes states, the high frequency state and the low-frequency state, respectively. It should be emphasized that the modes in a conventional whispering gallery cavity can be classified into two categories: standing modes and traveling modes [43]. However, despite the CTWG cavity having  $C_6$  symmetry, all modes in this cavity are traveling modes due to the forbidding counterpropagating modes. To confirm this, Figs. 5(c) and 5(d) display the Poynting vector distribution for the second-order mode, revealing that the Poynting vectors for both the second (eigenfrequency  $\omega_2 = 4.122$  GHz) and 2' CTWG modes

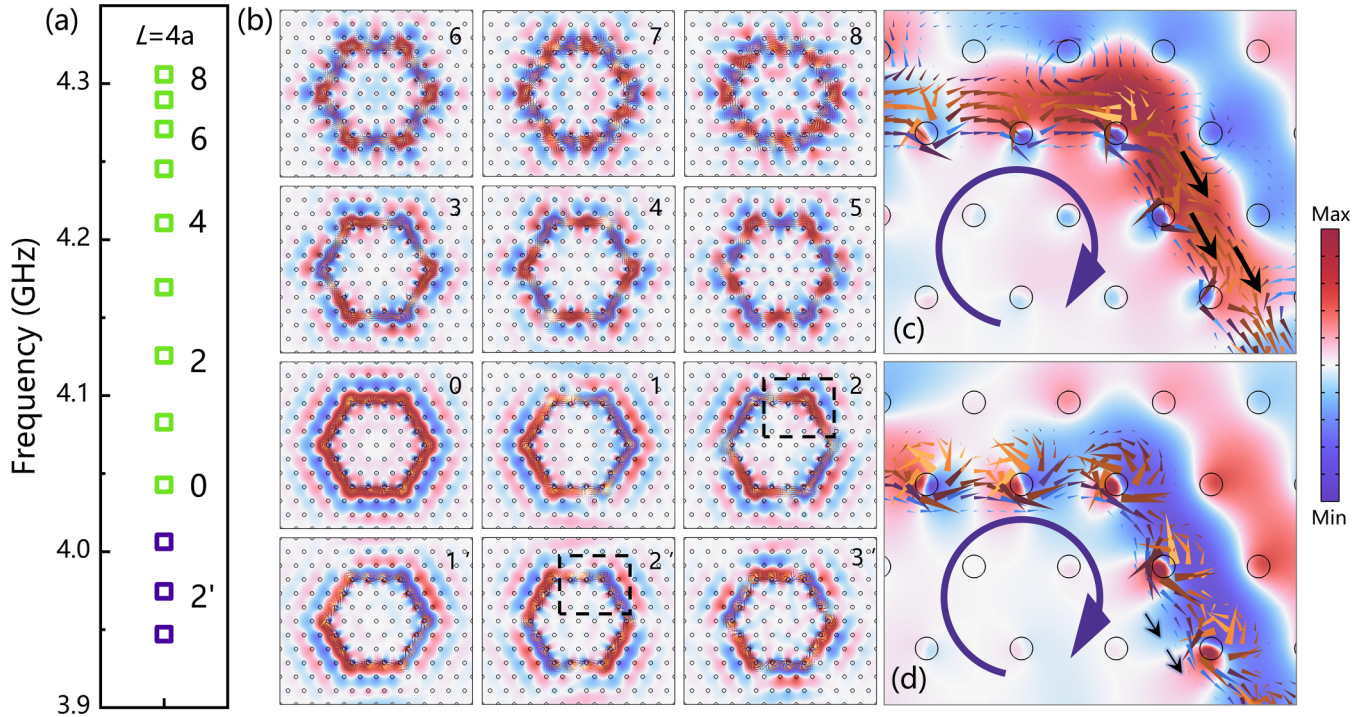


FIG. 5. Mode analysis of CTWG cavity. (a) Frequency spectrum of CTWG cavity with side length  $L = 4a$  contains 12 CTWG modes. The discrete CTWG modes labeled by the number of azimuthal modes. (b)  $E_z$  field distributions for all the CTWG modes are shown; the colors red and blue are used to indicate the relative phase of a field. (c),(d) Enlarged view of the second (c) and  $2'$  (d) clockwise modes, where the arrows indicate the distribution of time-averaged Poynting vector for the CTWG mode.

(eigenfrequency  $\omega_{2'} = 3.974$  GHz) exhibit a clockwise flow characteristic along the cavity, which is consistent with the direction of the CES shown in Fig. 3(a). Furthermore, it is worth noting that the second CTWG mode (high-frequency state) exhibits a greater concentration of clockwise mode fields in topological interface band between the trivial and nontrivial pillars compared to the  $2'$  CTWG mode (lower-frequency state). In contrast, the field energy in the low-frequency state is concentrated around the MOPC dielectric pillars within the nontrivial side. As per the energy variational principle [44], it is well established that the cavity mode tends to concentrate the majority of its electric field energy in the high dielectric constant region to minimize its frequency. Moreover, it is also important to note that the upper-frequency band must be orthogonal to the lower-frequency band. The  $2'$  mode achieves lower frequencies by concentrating the clockwise mode on the inner side of the interface. In contrast, the second mode, which is symmetric to the low-frequency state, shifts the clockwise mode towards the trivial photonic crystal and into the topological interface to maintain orthogonality with the  $2'$  mode. This is the reason why the seventh CTWG mode exhibits a high transmission peak, while the eighth mode has reduced transmission due to its frequency being outside the topological band gap [Fig. 3(e)].

In the case of this cavity, the number of CTWG modes increases as the length of the cavity increases. As we increase the size of the cavity, additional modes move from the bulk band to the edge state, as demonstrated in Eq. (4). As the cavity length increases from  $4a$  to  $5a$ , the number of CTWG modes, shown in Fig. 6(a), increases from 12 to 16.

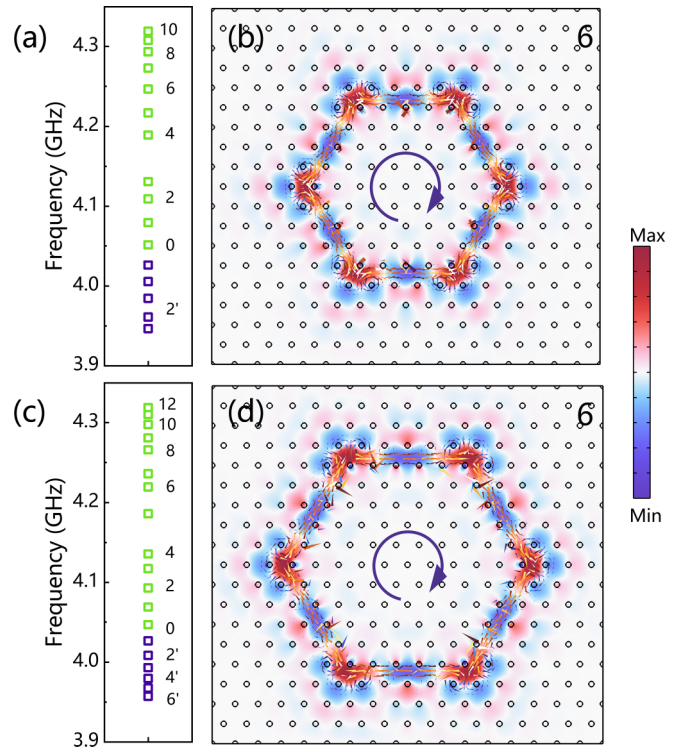


FIG. 6. CTWG mode distribution at different cavity lengths. The discrete CTWG modes labeled by numbers calculated with  $L = 5a$  (a), and  $L = 6a$  (b) respectively. (c),(d) The sixth  $E_z$  field and Poynting vector distribution of the corresponding cavity length show a clockwise traveling mode.



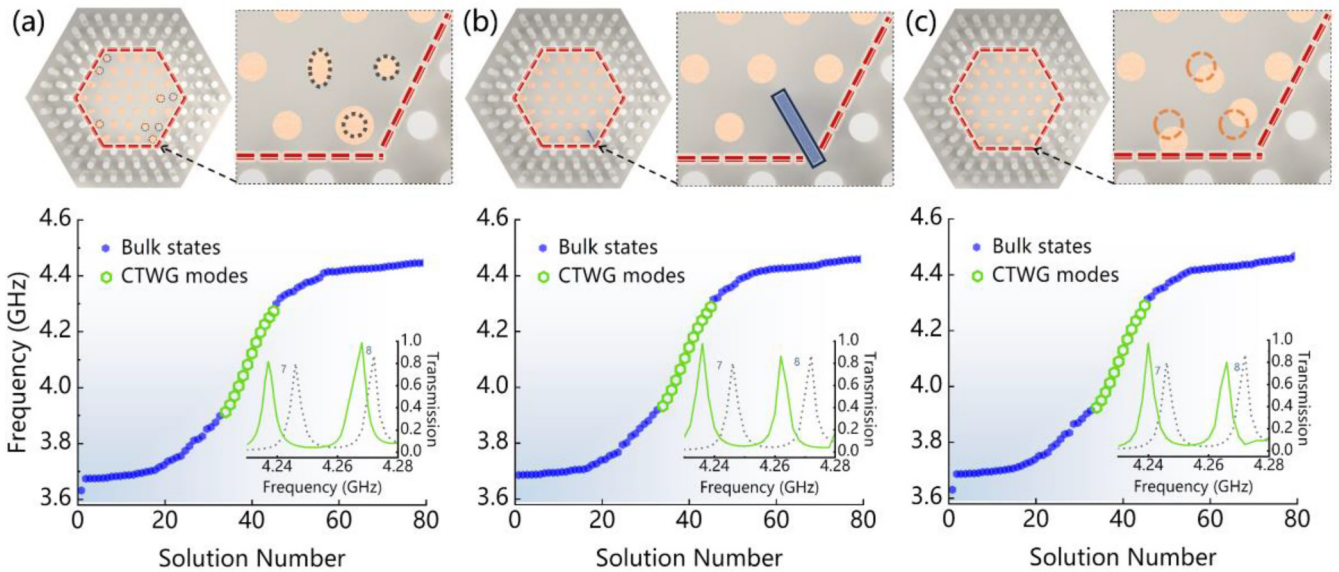


FIG. 7. Topological protection characteristics of whispering gallery modes. (a) Eigenspectra of the CTWG cavity with the disorders of dielectric pillars size. The inset indicates the location of the disordered unit cells. (b) Eigenspectra of CTWG cavity containing defects and contaminants; the blue areas indicate impurities at defects. (c) Eigenspectra of CTWG cavity under positional disorder. The transmission spectrum inset gives the frequency shift of the seventh and eighth order CTWG modes under the three types of strong perturbations.

Similarly, for a cavity with an edge length of  $6a$ , the band gap contains 19 modes, as depicted in Fig. 6(c). Even if the length of the cavity is increased, the CTWG mode still maintains the clockwise traveling wave characteristics, as shown in Figs. 6(c) and 6(d) (taking the sixth-order mode as an example). However, for cavities smaller than  $4a$ , the CTWG modes will disappear because there is not enough bulk to support the generation of edge states unless the lattice constant becomes even smaller. Therefore, the number of CTWG modes is completely geometrically dependent. This effect has been predicted in photonic topological insulator strips [6].

#### D. Robustness of CTWG modes

Robustness refers to the ability of a system to maintain its stability and reliability in the face of external interference or internal changes. The ability to maintain robustness against certain types of disorder under necessary symmetry protection is a remarkable feature of topological photonic systems. To investigate the topological protection properties of these CTWG cavity modes, we examined an array of cavities with a length of  $4a$  and introduced random variations in the magnitudes of the dielectric pillar radii of the nontrivial unit cells, isotropically and anisotropically. The eigenspectra of the cavity are calculated in the presence of pillar radius disorder, as shown in Fig. 7(a) and the inset of the transmission spectrum. The results show that under this type of perturbation, even though the CTWG mode resonance peaks show a slight frequency detuning compared to the perfect cavity mode transmission (gray dashed line in the inset), all modes are still present within the topological band gap and the robust transmission of the modes is maintained, which agrees with the findings in Fig. 5(a).

Next, a strong symmetry-breaking perturbation was induced by introducing defects and impurities in the cavity. The eigenspectrum of the CTWG modes under this condition was plotted in Fig. 3(e); similarly, frequency detuning of the cavity modes and robust transmission are observed. Figure 7(c) illustrates the eigenspectrum of the cavity with introduced disorder at the unit cell locations. It was observed that the spectral profile's line shape closely matches that of the unperturbed state, and both configurations support an equivalent number of CTWG modes. The reason for the frequency detuning of the CTWG mode may arise from defective impurities increasing the effective length of the cavity. Nevertheless, the topologically protected coupling between the edge states and the whispering gallery modes persists despite any potential perturbations. This affirms the topological protection of the CTWG modes to a considerable extent.

### III. METHODS

#### A. FEM simulation

Numerical simulations are performed using a commercial finite-element simulation software (COMSOL MULTIPHYSICS) via the Optical module. The band structures are simulated for the 2D transverse magnetic mode (i.e., the electric field is perpendicular to the 2D plane, along the  $z$  direction). The projected band diagram is calculated by simulating the eigenfrequencies of a semi-infinite topological nontrivial lattice, while the transmission spectra of the CES and CTWG modes are calculated in 3D photonic crystals with  $21 \times 8$  and 12 unit cells, depicted in Fig. 3. Mode analysis in Fig. 5 is performed on the 3D CTWG cavity and the wave vector is set as  $k = 0$ . The calculation of the Poynting vector is based on electromagnetic field simulations in the frequency domain, which were obtained using COMSOL port boundary.

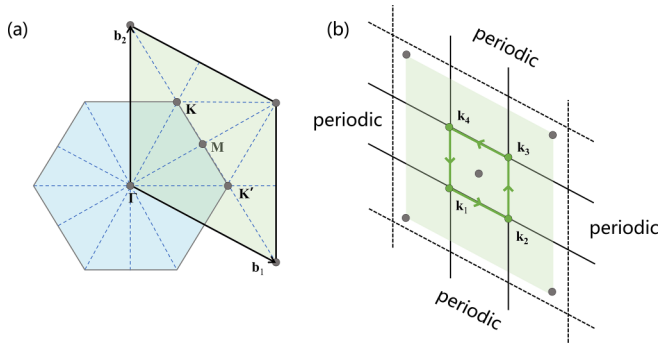


FIG. 8. Computational scheme for the calculation of Chern numbers. (a) For the convenience of  $K$ -space discretization, the hexagonal Brillouin zone (blue region) is equivalently replaced by the rhombic Brillouin zone (green region) with high-symmetry points ( $\Gamma$ ,  $M$ ,  $K$ , and  $K'$ ) indicated. (b) Discretized Brillouin zone. The line elements highlighted in green represent a Wilson loop that surrounds the  $M$  point.

### B. Chern number calculation

The topological invariants of the  $n$ th nondegenerate band of a magneto-optical photonic crystal with a triangular lattice are described by the Chen number for the discrete Brillouin zone as shown in Fig. 8, and thus the Chern number can be calculated by using [20]

$$\begin{aligned}
 C^{(n)} &= \frac{1}{2\pi} \int_{\text{BZ}} \mathbf{F}_n(\mathbf{k}) d\mathbf{k} \\
 &= \frac{1}{2\pi i} \oint_{\partial \text{BZ}} \langle \mathbf{u}_{n,e,\mathbf{k}} | \nabla_{\mathbf{k}} | \mathbf{u}_{n,e,\mathbf{k}} \rangle d\mathbf{k} \\
 &= \frac{1}{2\pi} \sum_{\mathbf{k} \in \text{BZ}} F_{\mathbf{k}}^{(n)} \Delta S_{\mathbf{k}} \\
 &= \frac{1}{2\pi} \sum_{\mathbf{k} \in \text{BZ}} \text{Im} \ln [U_{\mathbf{k}_1 \rightarrow \mathbf{k}_2}^{(n)} U_{\mathbf{k}_2 \rightarrow \mathbf{k}_3}^{(n)} U_{\mathbf{k}_3 \rightarrow \mathbf{k}_4}^{(n)} U_{\mathbf{k}_4 \rightarrow \mathbf{k}_1}^{(n)}], \quad (3)
 \end{aligned}$$

where  $U_{\mathbf{k}_\alpha \rightarrow \mathbf{k}_\beta}^{(n)} \equiv \frac{\langle \mathbf{u}_{n,e,\mathbf{k}_\alpha} | \mathbf{u}_{n,e,\mathbf{k}_\beta} \rangle}{|\langle \mathbf{u}_{n,e,\mathbf{k}_\alpha} | \mathbf{u}_{n,e,\mathbf{k}_\beta} \rangle|}$  is a  $U(1)$  link variable, and  $|\mathbf{u}_{n,e,\mathbf{k}}\rangle$  is the normalized eigenstate of the electric field, which satisfies the Bloch theorem [45,46], and  $\alpha, \beta = 1, 2, 3, 4$ ,  $\mathbf{k}_1,$

$\mathbf{k}_2, \mathbf{k}_3, \mathbf{k}_4$  are the vertices of any discrete Brillouin zone mesh [Fig. 8(b)].

### IV. CONCLUSION

In summary, we have constructed a CTWG cavity by using topological nontrivial photonic crystals surrounded by trivial PCs, where each mode is a one-way unidirectional traveling mode. We investigated the CES energy band structure and topological properties. Then a comprehensive investigation on the coupling characteristics between the CES and the whispering gallery cavity in the microwave regime was performed, which reveals that the originally continuous topological edge states evolved into multiple discrete nondegenerate whispering gallery modes in the cavity, with the number of modes only related to the circumference of the topological whispering gallery cavity. The CES guarantees that the wave can only propagate in one way, and thus in the CTWG cavity, only traveling modes exist. The high-frequency states concentrated in the topological interface band has extremely high transmission efficiency, which differs from whispering gallery cavities that support both traveling and standing waves. We further investigate the robustness of the CTWG modes derived from topological protection. Numerical simulations demonstrated that the coupling between edge states and cavities remained robust even in the presence of significant disorder. This means that the CTWG cavity can maintain stability and reliability in the face of external interference or internal changes, making it a promising candidate for various applications, allowing for the discovery and implementation of fruitful physical phenomena and useful functionalities.

### ACKNOWLEDGMENT

The authors acknowledge the support of the National Natural Science Foundation of China (Grants No. 12074054 and No. 12274054).

Y.F. conceived the idea and directed the project. Y.C. performed the FEM calculations. Y.C. and Y.F. analyzed the data and wrote the manuscript. All the authors revised the manuscript.

The authors declare no competing financial interest.

- 
- [1] S. Raghu and F. D. M. Haldane, Analogs of quantum-hall-effect edge states in photonic crystals, *Phys. Rev. A* **78**, 033834 (2008).
- [2] L. Lu, J. D. Joannopoulos, and M. Soljačić, Topological photonics, *Nat. Photonics* **8**, 821 (2014).
- [3] M. S. Rider, S. J. Palmer, S. R. Pooock, X. Xiao, P. Arroyo Huidobro, and V. Giannini, A perspective on topological nanophotonics: Current status and future challenges, *J. Appl. Phys.* **125**, 12 (2019).
- [4] F. Liu, H.-Y. Deng, and K. Wakabayashi, Topological photonic crystals with zero berry curvature, *Phys. Rev. B* **97**, 035442 (2018).
- [5] Z. Zhang, J. Yang, T. Du, and X. Jiang, Topological multipolar corner state in a supercell metasurface and its interplay with two-dimensional materials, *Photonics Res.* **10**, 855 (2022).
- [6] L.-H. Wu and X. Hu, Scheme for achieving a topological photonic crystal by using dielectric material, *Phys. Rev. Lett.* **114**, 223901 (2015).
- [7] S. Han, J. Cui, Y. Chua, Y. Zeng, L. Hu, M. Dai, F. Wang, S. Zhu, L. Li *et al.*, Electrically-pumped compact topological bulk lasers driven by band-inverted bound states in the continuum, *Light Sci. Appl.* **12**, 145 (2023).
- [8] B. Hu, Z. Zhang, H. Zhang, L. Zheng, W. Xiong, Z. Yue, X. Wang, J. Xu, Y. Cheng, X. Liu *et al.*, Non-hermitian topological whispering gallery, *Nature (London)* **597**, 655 (2021).
- [9] M. Z. Hasan and C. L. Kane, Colloquium: Topological insulators, *Rev. Mod. Phys.* **82**, 3045 (2010).

- [10] X.-L. Qi and S.-C. Zhang, Topological insulators and superconductors, *Rev. Mod. Phys.* **83**, 1057 (2011).
- [11] B. A. Bernevig and S.-C. Zhang, Quantum spin Hall effect, *Phys. Rev. Lett.* **96**, 106802 (2006).
- [12] M. A. Bandres, S. Wittek, G. Harari, M. Parto, J. Ren, M. Segev, D. N. Christodoulides, and M. Khajavikhan, Topological insulator laser: Experiments, *Science* **359**, 6381 (2018).
- [13] G. Siroki, P. A. Huidobro, and V. Giannini, Topological photonics: From crystals to particles, *Phys. Rev. B* **96**, 041408(R)(2017).
- [14] Y. Chen, X.-T. He, Y.-J. Cheng, H.-Y. Qiu, L.-T. Feng, M. Zhang, D.-X. Dai, G.-C. Guo, J.-W. Dong, and X.-F. Ren, Topologically protected valley-dependent quantum photonic circuits, *Phys. Rev. Lett.* **126**, 230503 (2021).
- [15] Y. Zeng, U. Chattopadhyay, B. Zhu, B. Qiang, J. Li, Y. Jin, L. Li, A. G. Davies, E. H. Linfield, B. Zhang *et al.*, Electrically pumped topological laser with valley edge modes, *Nature (London)* **578**, 246 (2020).
- [16] X. Wu, Y. Meng, J. Tian, Y. Huang, H. Xiang, D. Han, and W. Wen, Direct observation of valley-polarized topological edge states in designer surface plasmon crystals, *Nat. Commun.* **8**, 1304 (2017).
- [17] L. Esaki, *Highlights in Condensed Matter Physics and Future Prospects* (Springer, New York, 2013).
- [18] Z. Wang, Y. D. Chong, J. D. Joannopoulos, and M. Soljačić, Reflection-free one-way edge modes in a gyromagnetic photonic crystal, *Phys. Rev. Lett.* **100**, 013905 (2008).
- [19] Z. Wang, Y. Chong, J. D. Joannopoulos, and M. Soljačić, Observation of unidirectional backscattering-immune topological electromagnetic states, *Nature (London)* **461**, 772 (2009).
- [20] D. Jin, T. Christensen, M. Soljačić, N. X. Fang, L. Lu, and X. Zhang, Infrared topological plasmons in graphene, *Phys. Rev. Lett.* **118**, 245301 (2017).
- [21] Babak Bahari, A. Ndao, F. Vallini, A. El Amili, Y. Fainman, and B. Kanté, Nonreciprocal lasing in topological cavities of arbitrary geometries, *Science* **358**, 636 (2017).
- [22] J. Chen, W. Liang, and Z.-Y. Li, Strong coupling of topological edge states enabling group-dispersionless slow light in magneto-optical photonic crystals, *Phys. Rev. B* **99**, 014103 (2019).
- [23] K. Fang, Z. Yu, and S. Fan, Realizing effective magnetic field for photons by controlling the phase of dynamic modulation, *Nat. Photonics* **6**, 782 (2012).
- [24] C. He, X.-C. Sun, X.-P. Liu, M.-H. Lu, Y. Chen, L. Feng, and Y.-F. Chen, Photonic topological insulator with broken time-reversal symmetry, *Proc. Natl. Acad. Sci. USA* **113**, 4924 (2016).
- [25] L. Lu, H. Gao, and Z. Wang, Topological one-way fiber of second chern number, *Nat. Commun.* **9**, 5384 (2018).
- [26] S. Yang, Y. Wang, and H. Sun, Advances and prospects for whispering gallery mode microcavities, *Adv. Opt. Mater.* **3**, 1136 (2015).
- [27] K. J. Vahala, Optical microcavities, *Nature (London)* **424**, 839 (2003).
- [28] Y. Zhi, X.-C. Yu, Q. Gong, L. Yang, and Y.-F. Xiao, Single nanoparticle detection using optical microcavities, *Adv. Mater.* **29**, 12 (2017).
- [29] J. Wiersig, Structure of whispering-gallery modes in optical microdisks perturbed by nanoparticles, *Phys. Rev. A* **84**, 063828 (2011).
- [30] J. A. Haigh, S. Langenfeld, N. J. Lambert, J. J. Baumberg, A. J. Ramsay, A. Nunnenkamp, and A. J. Ferguson, Magneto-optical coupling in whispering-gallery-mode resonators, *Phys. Rev. A* **92**, 063845 (2015).
- [31] Y. Yang and Z. H. Hang, Topological whispering gallery modes in two-dimensional photonic crystal cavities, *Opt. Express* **26**, 21235 (2018).
- [32] L. He, W. X. Zhang, and X. D. Zhang, Topological all-optical logic gates based on two-dimensional photonic crystals, *Opt. Express* **27**, 25841 (2019).
- [33] A. Dikopoltsev, T. H. Harder, E. Lustig, O. A. Egorov, J. Beierlein, A. Wolf, Y. Lumer, M. Emmerling, C. Schneider, S. Höfling *et al.*, Topological insulator vertical-cavity laser array, *Science* **373**, 1514 (2021).
- [34] M.-S. Wei, M.-J. Liao, C. Wang, C. Zhu, Y. Yang, and J. Xu, Topological laser with higher-order corner states in the two-dimensional su-schrieffer-heeger model, *Opt. Express* **31**, 3427 (2023).
- [35] Y. Gong, S. Wong, A. J. Bennett, D. L. Huffaker, and S. S. Oh, Topological insulator laser using valley-hall photonic crystals, *ACS Photonics* **7**, 2089 (2020).
- [36] Y. Ota, R. Katsumi, K. Watanabe, S. Iwamoto, and Y. Arakawa, Topological photonic crystal nanocavity laser, *Commun. Phys.* **1**, 86 (2018).
- [37] X.-C. Sun and X. Hu, Topological ring-cavity laser formed by honeycomb photonic crystals, *Phys. Rev. B* **103**, 245305 (2021).
- [38] COMSOL - Software for Multiphysics Simulation, <https://www.comsol.com/>.
- [39] S. A. Skirlo, L. Lu, and M. Soljačić, Multimode one-way waveguides of large chern numbers, *Phys. Rev. Lett.* **113**, 113904 (2014).
- [40] S. A. Skirlo, L. Lu, Y. Igarashi, Q. Yan, J. Joannopoulos, and M. Soljačić, Experimental observation of large chern numbers in photonic crystals, *Phys. Rev. Lett.* **115**, 253901 (2015).
- [41] Y. Poo, R. X. Wu, Z. Lin, Y. Yang, and C. T. Chan, Experimental realization of self-guiding unidirectional electromagnetic edge states, *Phys. Rev. Lett.* **106**, 093903 (2011).
- [42] X. Ao, Z. Lin, and C. T. Chan, One-way edge mode in a magneto-optical honeycomb photonic crystal, *Phys. Rev. B* **80**, 033105 (2009).
- [43] Q. Li, T. Wang, Y. Su, M. Yan, and M. Qiu, Coupled mode theory analysis of mode-splitting in coupled cavity system, *Opt. Express* **18**, 8367 (2010).
- [44] *Photonic Crystals: Molding the Flow of Light*, 2nd ed., edited by J. D. Joannopoulos (Princeton University Press, Princeton, 2008).
- [45] T. Fukui, Y. Hatsugai, and H. Suzuki, Chern numbers in discretized brillouin zone: Efficient method of computing (spin) hall conductances, *J. Phys. Soc. Jpn.* **74**, 1674 (2005).
- [46] R. Zhao, G.-D. Xie, M. L. N. Chen, Z. Lan, Z. Huang, and W. E. I. Sha, First-principle calculation of chern number in gyrotropic photonic crystals, *Opt. Express* **28**, 4638 (2020).